OPEN ACCESS

University of BRISTOL

Tkáč, O., Saha, A. K., Loreau, J., Ma, Q., Dagdigian, P. J., Parker, D., Van Der Avoird, A., & Orr-Ewing, A. J. (2015). Rotationally inelastic scattering of ND_3 with H_2 as a probe of the intermolecular potential energy surface. *Molecular Physics*, *113*(24), 3925-3933. https://doi.org/10.1080/00268976.2015.1059958

Peer reviewed version

Link to published version (if available):
10.1080/00268976.2015.1059958

Link to publication record in Explore Bristol Research
PDF-document

This is an Accepted Manuscript of an article published by Taylor & Francis in Molecular Physics in December 2015, available online: http://www.tandfonline.com/doi/full/10.1080/00268976.2015.1059958.

University of Bristol - Explore Bristol Research
General rights

This document is made available in accordance with publisher policies. Please cite only the published version using the reference above. Full terms of use are available:
http://www.bristol.ac.uk/red/research-policy/pure/user-guides/ebr-terms/

Rotationally inelastic scattering of ND_3 with H_2 as a probe of the intermolecular potential energy surface

Ondřej Tkáč,[a] Ashim K. Saha,[b] Jérôme Loreau,[c] Qianli Ma (马千里),[d†] Paul J. Dagdigian,*[d] David H. Parker,*[b] Ad van der Avoird,*[b] and Andrew J. Orr-Ewing[e]

[a] *Laboratorium für Physikalische Chemie, ETH Zürich, CH-8093 Zürich, Switzerland*

[b] *Radboud University Nijmegen, Institute for Molecules and Materials, Heyendaalseweg 135, 6525 AJ Nijmegen, The Netherlands*; E-mail: parker@science.ru.nl, avda@theochem.ru.nl

[c] *Service de Chimie Quantique et Photophysique, Université Libre de Bruxelles (ULB) CP 160/09, 50 av. F.D. Roosevelt, 1050 Brussels, Belgium*

[d] *Department of Chemistry, The Johns Hopkins University, Baltimore, Maryland 21218-2685, USA;* E-mail: pjdagdigian@jhu.edu

[e] *School of Chemistry, University of Bristol, Cantock's Close, Bristol BS8 1TS, UK*

† Present address: *Institut für Theoretische Chemie, Universität Stuttgart, Pfaffenwaldring 55, D-70569 Stuttgart, Germany*

Abstract

Differential cross sections are reported for rotationally inelastic scattering of ND_3 with H_2, measured using a crossed molecular beam apparatus with velocity map imaging (VMI). ND_3 molecules were quantum-state selected in the ground electronic and vibrational levels and, optionally, in the $j_k^{\pm} = 1_1^-$ rotation-inversion level prior to collisions. Inelastic scattering of state-selected ND_3 with H_2 was measured at a mean collision energy of 580 cm^{-1} by resonance enhanced multiphoton ionization spectroscopy and VMI of ND_3 in selected single final $j'^{\pm}_{k'}$ levels. Comparison of experimental differential cross sections with close-coupling quantum-mechanical scattering calculations serves as a test of a recently reported *ab initio* potential energy surface. Calculated integral cross sections reveal the propensities for scattering into various final $j'^{\pm}_{k'}$ levels of ND_3 and differences between scattering by *ortho* and *para* H_2. Integral and differential cross sections are also computed at a mean collision energy of 430 cm^{-1} and compared to our recent results for inelastic scattering of state-selected ND_3 with He.

I. Introduction

Rotationally inelastic scattering of ammonia isotopologues has attracted recent attention because of its astrophysical importance [1,2]. Ammonia was discovered in the interstellar medium by observing emissions at a frequency corresponding to the inversion transitions of the rotational levels $j_k = 1_1$ and 2_2 in the vibrational ground state of NH_3 [3]. Fully deuterated ammonia, ND_3, has since been observed in prestellar cores [4]. Deuterium-bearing molecules are important as probes of the very cold phases of molecular clouds, prior to star formation, and the isotopic compositions of molecules provide clues to their formation mechanisms [5]. The $j_k = 3_3$ inversion transition of NH_3 has been predicted [6] and observed [7] to exhibit maser activity. Because gas-phase collisions can transfer population to higher-lying rotational levels, inelastic scattering experiments and calculations help interpret the anomalous non-thermal microwave radiation emitted from interstellar clouds.

Previous studies of ammonia scattering were mostly restricted to measurement of integral cross sections (or rate coefficients) [8-10]. Differential cross sections (DCSs) for inelastic scattering of NH_3 with n-H_2 were measured by Meyer [11] using counter-propagating molecular beams at a collision energy of 1177 cm^{-1}. Experimental and theoretical DCSs have also been reported for NH_3–He [12,13] and NH_3–Ar [13,14] collisions, as well as experimental DCSs for ND_3–Ne scattering [15]. These measurements and calculations were performed without selection of the inversion symmetry of the initial state associated with the umbrella vibrational mode. Recently, we reported inelastic scattering studies of ND_3 with He [16] and Ar [17], with full selection of the initial state, including this inversion symmetry, and found excellent agreement with close coupling quantum mechanical (QM) scattering calculations. Excellent agreement was also obtained between velocity map imaging (VMI) data and QM scattering calculations for inelastic scattering of CD_3 radicals with He [18], H_2 and D_2 [19] and Ar [20]. The rotationally inelastic scattering dynamics of deuterated ammonia and methyl radicals in collisions with helium were recently compared, using close-coupling QM scattering calculations performed with accurate *ab initio* potential energy surfaces [21].

In the current study, molecular hydrogen was selected as a collision partner for ND_3 because of its high abundance in the universe, and hence astrophysical significance as a collider. Molecular hydrogen is recognized as a major contributor to the cooling of astrophysical media [22]. Accurate computed DCSs for ammonia collisions involving the H_2 molecule are computationally tractable because the large rotational constant means that only a few rotational levels of the collision partner need to be included in QM scattering calculations. The diatomic H_2 molecule, with its rotational degrees of freedom, adds complexity to the scattering dynamics when compared to recent studies of ND_3 collisions with Ar and He.

Para-H_2 in the rotational ground state with rotational quantum number $j_2 = 0$ is considered to be similar to a He atom in its interaction with ammonia because of the absence

of a dipole-quadrupole interaction. However, Schleipen *et al*. [10] showed that for some rotational levels of NH_3, the results of scattering for *para*-H_2 (j_2= 0) are different than for He. Our current experiment does not distinguish between *ortho* and *para* H_2, but the theoretical calculations enable us to draw conclusions about differences between *ortho* (j_2= 1, 3, …) and *para* (j_2= 0, 2, …) integral and differential cross sections.

Our collision energies (580 cm^{-1}) are larger than those expected for typical astrophysical conditions [8]; nevertheless, the comparison between experiment and theory provides a test of a recently reported *ab initio* potential energy surface (PES) [23] that can be used in calculations corresponding to the lower collision energy regime. The experimental study of ammonia collisions at lower energies is also now accessible using a Stark decelerator to slow the ammonia molecules. Low energy collisions of NH_3 with He were studied theoretically by Gubbels *et al*. [24] with a focus on the observation of scattering resonances and revealed diffraction oscillations in the small-angle scattering regions of the DCSs. These types of interference structures are beyond the resolution of the current experiments, but can in principle be resolved using a Stark decelerated molecular beam, as shown recently for inelastic collisions of NO with He, Ne and Ar [25,26].

The current work seeks to explore the dynamics of translational to rotational energy transfer in collisions of ND_3 with H_2 and therefore to understand better the intermolecular interactions. Measurements are reported of quantum-state resolved DCSs obtained using crossed molecular beam (CMB) scattering, combined with resonance enhanced multi-photon ionization (REMPI) detection and velocity-map imaging [27]. The state-to-state DCSs were measured for scattering of ND_3 in its ground electronic ($\tilde{X}^1A_1'$) and vibrational (v = 0) levels from H_2:

$$ND_3\,(\tilde{X}, v = 0, j_k^{\pm} = 1_1^-) + H_2\,(j_2) \rightarrow ND_3\,(\tilde{X}, v' = 0, j'^{\pm}_{k'}) + H_2\,(j_2') \qquad (1)$$

with $j' \leq 4$, $k' \leq 4$, and +/– denoting symmetry / asymmetry of the inversion state associated with the ν_2 umbrella vibrational mode. Initial state selection of $j_k^{\pm} = 1_1^-$ was achieved by passing a supersonically expanded and cooled molecular beam of ND_3 in an inert carrier gas through a hexapole state selector. Measurements were also performed without the hexapole filter, with the initial state of the ND_3 averaged over +/– symmetry components and several j_k levels. Measured DCSs are compared to the outcomes of QM scattering calculations, providing stringent tests of the accuracy of the *ab initio* computed PES.

II. Method

A. Experimental apparatus

The crossed molecular beam machine located in the Nijmegen laboratory was described in detail previously [16], and we present only a brief summary here. A home-built pulsed (Peter) valve [28] was used to produce a primary molecular beam of a mixture of 1% ND_3 seeded in argon. The secondary H_2 beam resulted from supersonic expansion of the pure gas through a hairpin-type Jordan pulsed valve. The opening times and the repetition rates of both valves were 100 μs and 10 Hz, respectively. Both molecular beams were collimated by skimmers with 3-mm diameters. The ND_3 primary beam then passed through a pair of 12-cm long hexapoles operating at 18.5 kV to ensure initial state selection. Alternatively, a different source chamber could be used to produce a primary ND_3 beam without hexapole state selection. The H_2 beam was characterized previously by (3+1) REMPI spectroscopy and had a rotational temperature of 220 K; for normal H_2 the only significantly populated rotational levels were those with j_2 = 0, 1 and 2 [29]. The primary and secondary beams intersected at 90^o inside a high vacuum chamber with a base pressure of 3×10^{-7} mbar. The pressure during experimental measurements was maintained at 2×10^{-6} mbar.

The ND_3 molecules were scattered in a single collision with H_2 into various $j'^{\pm}_{k'}$ final rotational levels. The scattered ND_3 molecules were state-selectively ionized by (2+1) REMPI via the v_2 = 4 or 5 vibrational levels of the $\tilde{B}$ Rydberg electronic state. The laser system used to produce ultraviolet wavelengths of 321‑322 nm and 317‑318 nm consisted of a tuneable pulsed dye laser (Lambda Physik ScanMate) pumped by a Nd:YAG laser (Continuum Powerlite 9000), with frequency doubling of the fundamental output of the dye laser. Typical UV laser energies were 4.5 mJ/pulse with 10 Hz repetition rate.

Collisions between particles in the primary and secondary beams occurred at the centre of an electrode assembly designed for velocity map imaging. The expanding Newton sphere of ND_3^+ ions prepared by REMPI of scattered ND_3 was extracted by a set of ion optics toward a position sensitive detector. This detector consisted of a pair of microchannel plates in chevron configuration located in front of a phosphor screen viewed by a CCD camera. The VMI ion optics comprised a repeller, an extractor, and a grounded electrode. The repeller voltage was maintained at 1 kV, and optimization of the extractor voltage to ±3 V around 777 V ensured circular and focused images. Under these velocity map imaging conditions, the radius of the recorded ion image was directly proportional to the speed of the ions at their point of formation by REMPI. More importantly for our current study, recorded velocity map images contained

information on the angular variation of the density of scattered ND_3 molecules, and hence could be analysed to obtain differential cross sections. The DCSs were extracted from experimental images using a density-to-flux transformation in the same way as described in our recent work [16,17]. This image analysis used an instrument function generated by a Monte Carlo simulation program [30] that incorporated numerous experimentally determined parameters characterizing the properties of the molecular and laser beams. These parameters included the speed and angular divergence distributions, temporal profiles, and spatial widths of the two molecular beams, as well as the Rayleigh range and beam waist of the focused probe laser. The Monte Carlo simulation program assumed Gaussian forms for these distributions and spatial and temporal profiles, and the experimentally determined FWHMs of all the Gaussian functions were used for density-to-flux conversion. In addition, the distances between the molecular beam sources and the scattering centre, which define the geometry of the experiment, are necessary parameters to determine the detection efficiency. By sampling ~2×10^8 sets of initial conditions from the Gaussian distributions of molecular beam and laser beam properties, the Monte Carlo program simulated the instrument function that determines the dependence of relative detection efficiencies on final laboratory frame velocities. Raw experimental images were processed by application of this instrument function. The DCSs were then extracted directly from the outer circumferences of the corrected images.

We discussed the rotational energy level structure of ND_3, nuclear spin effects and selection rules for spectroscopic transitions elsewhere [16]. At the rotational temperature of 4 K in the primary beam, only the three lowest energy rotational levels j_k = 0_0, 1_1 and 1_0 were significantly populated, with just 0.7% of population in higher rotational levels. The hexapole state selection further restricted the initial state of ND_3 to $j_k^{\pm} = 1_1^-$.

B. Quantum scattering calculations

Quantum scattering calculations of integral and differential cross sections for collision of the symmetric top ND_3 with the H_2 diatomic molecule were carried out in Nijmegen and Brussels with a scattering code developed in Nijmegen [21,24], and in Baltimore with the HIBRIDON suite of programs [31]. These calculations employed the five-dimensional NH_3–H_2 PES computed by Maret *et al.*[23], which depends on the coordinates $R, \theta_1, \phi_1, \theta_2, \phi_2$. Here, R is the magnitude of the vector **R** connecting the NH_3 and H_2 centers of mass, θ_1 is the angle between R and the C_3 axis of NH_3, ϕ_1 is the angle of rotation of this vector around the C_3 axis, and (θ_2, ϕ_2) are the polar and azimuthal angles used to describe the orientation of H_2 relative

to NH_3. For an illustration of the coordinates, see Fig. 2 of Rist *et al.*[32]. In the calculation of the PES, both molecules were assumed to be rigid rotors.

The PES was computed [23] with the coupled-cluster method with single, double, and perturbative triple excitations. It was constructed by calibrating the intermolecular energy obtained for a large set of geometries with the aug-cc-pVDZ basis set with a smaller set calculated with the aug-cc-pVTZ basis set. The accuracy of the PES was estimated to be on the order of 1 cm^{-1}.

We assume that the NH_3–H_2 and ND_3–H_2 interactions can be described by the same PES. The PES was computed with the N–H bond length set to the ground-state averaged value, which is slightly different in the case of ND_3, but the effect of the change in bond length is expected to be small [33]. On the other hand, it is necessary to take into account the shift in the position of the center of mass, which affects the definition of the coordinate system. The coordinates R' and θ_1' appropriate to ND_3–H_2 are easily expressed as functions of R and θ_1, similar to what was done in previous work on ND_3–He and ND_3–Ar [16,17,34], while the coordinates ϕ_1, θ_2, and ϕ_2 are left unchanged by the transformation.

For calculation of the matrix elements of the potential in the scattering basis, it is convenient to carry out an angular expansion. The PES was expanded in Nijmegen in terms of these new coordinates

$$V(R', \theta_1', \phi_1, \theta_2, \phi_2) = \sum_{l_1 l_2 l \mu_1} V_{l_1 l_2 l \mu_1}(R') t_{l_1 l_2 l \mu_1}(\theta_1', \phi_1, \theta_2, \phi_2) \,, \qquad (2)$$

where the angular functions $t_{l_1 l_2 l \mu_1}$ are given in Ref. [35]. The expansion coefficients $V_{l_1 l_2 l \mu_1}(R')$ were computed up to $l_1 = 11$ and $l_2 = 4$. A similar expansion [32] of the PES was carried out in Baltimore.

Since the PES does not describe the inversion of ND_3, the umbrella motion was treated with a two-state model in which the ground inversion-tunnelling states are taken as linear combinations of the two rigid equilibrium states. This model was shown to give good agreement with results obtained by treating the ND_3 umbrella motion explicitly in the case of NH_3–He and ND_3–He collisions [16,24].

State-to-state differential and integral cross sections were computed using the close-coupling method for the collision of a symmetric top with a linear molecule [36] for the initial rotational levels $j_k^{\pm} = 0_0^{\pm}, 1_0^{\pm}, 1_1^{\pm}$, of ND_3 and j_2 = 0, 1 and 2 of H_2. The latter set of initial levels allows comparisons with experimental measurements for which we assume the H_2 molecular beam contains a statistical mixture of j_2 = 0, 1 and 2 rotational levels. The only j_2-

changing transitions included in our DCS calculations were $j_2 = 0 \rightarrow 2$ and $j_2 = 2 \rightarrow 0$. The rotational constants were taken as A = 5.1432 cm^{-1}, C = 3.1015 cm^{-1}, and a j-independent inversion splitting of 0.0530 cm^{-1} for ND_3, and B = 59.3398 cm^{-1} for H_2. Cross sections were computed for two collision energies (430 and 580 cm^{-1}).

Convergence of the cross sections was checked with respect to the size of the rotational basis and the number of partial waves in the calculation. The rotational basis consisted of all rotational levels $j_1 \leq 8$ for ND_3 and $j_2 \leq 4$ for H_2. While the basis for ND_3 does not include all open channels at the energies considered here, it was truncated to reduce the computational time. An increase of the ND_3 basis set had no effect on the cross sections presented in this work. On the other hand, we found that truncating the basis for H_2 to $j_2 \leq 2$ caused changes of up to 25% in the state-to-state integral cross sections, and it was necessary to include closed channels up to $j_2 = 4$. The calculations included total angular momenta $J \leq 65\hbar$.

III. Results and Discussion

A. Differential cross sections for ND_3 (1_1^-) + n-H_2 scattering

Fig. 1 shows experimental images for inelastic scattering of hexapole state selected ND_3 from its $j_k^{\pm} = 1_1^-$ level into various final rotational levels $j'^{\pm}_{k'}$ following collision with n-H_2. The mean collision energy and the spread were 580 ± 50 cm^{-1}. The corresponding DCSs extracted using density-to-flux transformation are shown in Fig. 2 and are compared with calculated DCSs. For the purpose of comparison, the experimental DCSs were normalized to match the values of the theoretical DCSs at θ = 90°. The error bars associated with the experimental DCSs were determined by combining the standard deviation obtained from comparison of several measured images for a single final level with the uncertainty introduced by application of the density-to-flux transformation. They do not incorporate the angular resolution of the measurements (estimated to be 15^o in the forward scattering direction) or other potential sources of systematic error.

In general, the calculated DCSs agree well with the experimental measurements, except that we were not able to resolve experimentally the diffraction oscillations present at small scattering angles. The sharp peak present in some of the calculated DCSs at small angles (typically < 15^o) is also not reproduced well in our experiment because of imperfect subtraction of image contamination caused by the small fraction of ND_3 molecules present in the molecular beam in the probed quantum state. Some disagreement is evident between experiment and

theory for the amount of backward-scattered ND_3 (3_2^+) (Fig. 2(d)). This discrepancy may reflect problems associated with this experimental measurement, or subtle errors in the PES that manifest themselves in the scattering into this one final quantum state. The DCSs for final levels 2_1 and 3_1 with both + and − umbrella vibrational inversion symmetry peak in the forward hemisphere, with very little flux for $\theta > 45°$. The DCSs for scattering into these two final rotational levels differ in magnitude for the + and − symmetry components of the final level, but have very similar shapes. However, the angular distributions for + and − symmetry components of the 3_2 and 4_4 final levels also differ significantly in shape: the DCSs for the 3_2^- and 4_4^- levels peak in the forward hemisphere, whereas they peak in the backward hemisphere for the 3_2^+ and 4_4^+ final levels. Similar behaviour was observed for the 3_2 and 4_4 final levels with respect to + and − symmetry components for inelastic scattering of ND_3 with He [16].

B. Differential cross sections for +/− symmetry averaged ND_3 + n-H_2 scattering

We now contrast scattering of hexapole state selected $ND_3(1_1^-)$ with scattering into several ND_3 rotational levels from +/− symmetry and low-j_k averaged initial levels of ND_3. The initial-level population distribution for ND_3 without hexapole state selection is shown in Table 1 of Ref. [16]. The experimental images for a collision energy of 585 ± 50 cm^{-1} are shown in Fig. 3. The comparison of experimental and theoretical DCSs, presented as weighted sums of state-to-state DCSs over the initial-level distribution are shown Fig. 4. State selective detection was carried out solely through the $\tilde{B}(5)$ band, therefore the inversion symmetry of the final level for all measured images is −. The experimental DCSs were normalized to match values of theoretical DCSs at $\theta = 90°$. DCSs are not shown at small scattering angles, for which there is interference from unscattered and elastically scattered molecules present in the parent beam. Agreement between experiment and theory is satisfactory for scattering angles larger than $20 - 30^o$ where the state-averaged DCSs exhibit only broad structures.

C. ND_3 scattering with *ortho* and *para*-H_2

Molecular hydrogen consists of *para*-H_2 with total nuclear spin $I = 0$ and *ortho*-H_2 with nuclear spin $I = 1$. Even though our experiment does not distinguish between *ortho*- and *para*-H_2, theoretical calculations enable us to draw conclusions about differences between scattering of ND_3 by *ortho*- ($j_2 = 1, 3, \ldots$) and *para*- ($j_2 = 0, 2, \ldots$) H_2. Computed integral cross sections are shown in Fig. 5 for scattering of ND_3 out of the 1_1^- initial level into both symmetry components of the final level by H_2 initially in the $j_2 = 0$, 1 and 2 rotational level, for collisions that conserve j_2. ICSs for *para*-H_2 in its rotational ground state ($j_2 = 0$) are much smaller for

$\Delta k = 0$ transitions conserving the inversion symmetry of the ND_3 (thus, final levels 2_1^-, 3_1^-, …) than for collisions with rotationally excited H_2 ($j_2 = 1$ and 2). Indeed, only 18% of scattering with *para*-H_2($j_2 = 0$) results in $\Delta k = 0$ collisions, whereas this fraction is 50% for both $j_2 = 1$ and 2 rotational levels of H_2. Thus, rotating H_2 is more effective in conserving k in collisions. The reason that ground state *para*-H_2($j_2 = 0$) behaves differently in collisions than *ortho*-H_2($j_2 = 1$) and rotationally excited *para*-H_2($j_2 = 2$) is that the terms with $l_2 > 0$ in the expansion of the potential that depend on the orientation of H_2 average out in first order when $j_2 = 0$ and therefore do not play any direct role in the scattering for j_2 conserving collisions. Since ND_3 has a nonzero dipole moment, the leading electrostatic intermolecular interaction term is the dipole-quadrupole term, which falls off as R^{-4}. However, for ground state *para*-H_2 this interaction vanishes and the dipole-allowed transitions of ND_3 ($\Delta k = 0$, $\Delta j = \pm 1$) are expected to be smaller in collisions of ND_3 with *para*-H_2($j_2 = 0$) than in collisions with rotationally excited H_2. Note that the differences in ICSs between H_2 with $j_2 = 0$, 1 and 2 for collision changing the inversion symmetry of ND_3 (Fig. 5(b)) are smaller than those for collisions conserving the inversion symmetry and there are no clear trends. However, the $\Delta k = 0$ inversion-symmetry changing collisions still have smaller ICSs for *para*-H_2($j_2 = 0$).

Smaller ICSs for the $j_2 = 0$ than for the $j_2 = 1$ initial level of H_2 have also been observed for other molecule – H_2 scattering systems, e.g., NH_3–H_2 [23], OH–H_2 [37], and H_2O–H_2 [38]. In all these systems, the collision partners of H_2 have nonzero dipole moments so that the leading electrostatic term is the dipole-quadrupole interaction. This interaction corresponds to the $l_1 = 1$, $l_2 = 2$, $l = 3$ terms and can contribute to the cross sections for $j_2 = 1$ but not $j_2 = 0$ initial levels. In contrast, the ICSs for CD_3–H_2/D_2 collisions were found to be very similar for both $j_2 = 0$ and $j_2 = 1$ initial levels [19]. This observation is consistent with the methyl radical having no dipole moment, so that the dipole-quadrupole interaction is missing for CD_3–H_2/D_2 irrespective of rotational angular momentum of the H_2/D_2 collider.

The initial angular momentum of H_2 influences the ICSs of ND_3 scattering, and we now examine how it influences the scattering dynamics. For this purpose, we plot computed DCSs for selected final levels of ND_3 after collisions with H_2 with $j_2 = 0$, 1 and 2 in Fig. 6. The DCSs for 2_1^-, 2_1^+, 3_2^- and 4_4^- final levels have almost identical shapes for all three values of the H_2 rotational angular momentum. However, the DCSs for $j_2 = 0$ are different from the DCSs obtained for $j_2 = 1$ and 2 for the 3_2^+, 4_1^-, 4_1^+, and 4_4^+ final levels of ND_3. Interestingly the DCSs for $j_2 = 1$ and $j_2 = 2$ are almost identical for each final level (except in the case of the 3_2^+ final level for which small differences are observable), even though they involve scattering by *ortho*- and *para*-H_2, respectively. The differences in scattering dynamics of ND_3 with H_2 therefore seem not to be a consequence of *ortho* and *para* modification of H_2, but instead derive from scattering with rotationally excited and unexcited H_2.

D. Comparison of ND_3 scattering with H_2 and He

Para-H_2 in the rotational ground state with $j_2 = 0$ is expected to be similar to a He atom in its interaction with ammonia because of the absence of a dipole-quadrupole interaction. To compare ND_3 scattering with H_2 and He, we calculated ICSs and DCSs for ND_3–H_2 at a collision energy of 430 cm^{-1}, which was the collision energy for our recent study of the ND_3–He system [16]. Calculated ICSs for inelastic scattering of ND_3 with He and H_2 (j_2= 0 and 1) are shown in Fig. 7. The ICSs for scattering by p*ara*-H_2($j_2 = 0$) and He are different, especially for j'^{-}_{1} and 2^{+}_{1} final levels. For He as a collision partner only 21% of the total ICS involves umbrella mode inversion symmetry changing transitions [Fig.7(b)], whereas this fraction is 50% and 45% for H_2 with j_2= 0 and 1. However, this higher propensity for inversion symmetry-changing collisions for H_2 than for He is mostly accounted for by the larger ICS for the 2^{+}_{1} ND_3 final level for collisions involving H_2. In addition, Fig. 8 compares DCSs for He and *para*-H_2($j_2 = 0$) for selected ND_3 final levels, and we observe similar shapes for the DCSs for *para*-H_2($j_2 = 0$) and He as collision partners for ND_3.

IV. Conclusions

The inelastic scattering of quantum-state selected ND_3 with H_2 was examined experimentally in the Nijmegen laboratory. Fully state-to-state resolved DCSs for inelastic scattering of ND_3 ($\tilde{X}, \nu = 0, j_k^{\pm} = 1_1^-$) with H_2 at a collision energy of 580 cm^{-1} were compared to DCSs obtained by quantum mechanical scattering calculations performed with a previously reported *ab initio* PES. These comparisons were made for selected final rotational levels up to $j'_{k'} = 4_4$ and for both symmetric (+) and antisymmetric (–) components of the inversion vibration associated with the ν_2 umbrella mode of ND_3, and show satisfactory agreement between theory and experiment. However, the sharp peaks present in the calculated DCSs at small angles are not reproduced well in our experiments. Additional measurements and calculations were performed with the ND_3 initially state-averaged over several rotational levels as well as the +/– symmetry components. The resulting measured velocity map images are affected by imperfect subtraction of background signals caused by unscattered (and elastically scattered) ND_3 molecules in the molecular beam, especially for scattering angles $\theta \leq 15°$. Nevertheless, agreement between experiment and theory is satisfactory for scattering angles larger than 20 – 30° where the state-averaged DCSs exhibit only broad structures. The effectiveness of the hexapole selection of the initial quantum state and hence the purity of the state population in the molecular beam is demonstrated by these comparisons.

The DCSs are sensitive to the + or − symmetry component of the final level in certain, but not all cases. For example, the DCSs for the $1_1^- \rightarrow 3_2^-$ and 4_4^- transitions peak in the forward hemisphere, whereas they peak in the backward hemisphere for the 3_2^+ and 4_4^+ final levels. However, the DCSs for final levels with $j'_{k'} = 2_1$ and 3_1 with both + and − umbrella vibrational inversion symmetry are very similar, and all peak in the forward hemisphere. The analysis of computed ICSs and DCSs revealed that ground-state *para*-H_2 ($j_2 = 0$), which has zero total angular momentum, behaves differently in collisions than *ortho*-H_2 and rotationally excited *para*-H_2, because of the absence of a dipole-quadrupole interaction. The DCSs for collisions with H_2 (j_2= 1 and 2) are almost identical for each final level of ND_3 (except the 3_2^+ final level), whereas the DCSs for j_2= 0 are different from the DCSs obtained for j_2= 1 and 2 for the 3_2^+, 4_1^-, 4_1^+, and 4_4^+ final levels of ND_3. The differences in scattering dynamics of ND_3 with H_2 seem not to be a consequence of the *ortho* or *para* modification of H_2, but instead derive from scattering with rotationally excited and unexcited H_2 (or, more precisely, from the fact that ground state *para*-H_2 ($j_2 = 0$) has zero angular momentum).

Due to the absence of a dipole-quadrupole interaction, *para*-H_2 in the rotational ground state might be expected to be similar to a He atom in its interaction with ammonia. However, our theoretical calculations show that the ICSs for ND_3 (1_1^-) scattering by *para*-H_2 ($j_2 = 0$) and He differ, especially for transitions into j'^-_1 and 2_1^+ final levels. H_2 as a collision partner tends to promote umbrella mode inversion symmetry changing transitions more readily than He, but the DCSs for He and *para*-H_2($j_2 = 0$) exhibit similar shapes. Similar differences between NH_3 scattering with *para*-H_2 and with He were observed and discussed in Ref. [23].

Acknowledgements

The Nijmegen group acknowledges financial support from NWO-CW ECHO (for A.S.). The Bristol group thanks EPSRC for funding via the EPSRC Programme Grant EP/G00224X. These two groups were part of the EU Initial Training Network *ICONIC*, which provided financial support for O.T. and for visits between the two institutions. J.L. acknowledges support from the Belgian Fund for Scientific Research - FNRS and the Wiener-Anspach Foundation. P.J.D. and Q.M. acknowledge support from the U.S. National Science Foundation (grant no. CHE-1313332); they are also grateful for the advice and encouragement of Millard Alexander.

References

[1] U. Machin and E. Roueff, *J. Phys. B* **38**, 1519 (2005).

[2] W. F. Wang, *Chem. Phys.* **288**, 23 (2003).

[3] A. C. Cheung, D. M. Rank, C. H. Townes, D. D. Thornton, and W. J. Welch, *Phys. Rev. Lett.* **21**, 1701 (1968).

[4] E. Roueff, D. C. Lis, F. F. S. van der Tak, M. Gerin, and P. F. Goldsmith, *Astron. Astrophys.* **438**, 585 (2005).

[5] F. F. S. van der Tak, P. Schilke, H. S. P. Muller, D. C. Lis, T. G. Phillips, M. Gerin, and E. Roueff, *Astron. Astrophys.* **388**, L53 (2002).

[6] C. M. Walmsley and H. Ungerechts, *Astron. Astrophys.* **122**, 164 (1983).

[7] S. Guilloteau, T. L. Wilson, R. N. Martin, W. Batrla, and T. A. Pauls, *Astron. Astrophys.* **124**, 322 (1983).

[8] T. Seelemann, P. Andresen, J. Schleipen, B. Beyer, and J. J. ter Meulen, *Chem. Phys.* **126**, 27 (1988).

[9] J. Schleipen and J. J. ter Meulen, *Chem. Phys.* **156**, 479 (1991).

[10] J. Schleipen, J. J. ter Meulen, and A. R. Offer, *Chem. Phys.* **171**, 347 (1993).

[11] H. Meyer, *Mol. Phys.* **84**, 1155 (1995).

[12] H. Meyer, U. Buck, R. Schinke, and G. H. F. Diercksen, *J. Chem. Phys.* **84**, 4976 (1986).

[13] G. C. M. van der Sanden, P. E. S. Wormer, and A. van der Avoird, *J. Chem. Phys.* **105**, 3079 (1996).

[14] H. Meyer, *J. Chem. Phys.* **101**, 6697 (1994).

[15] J. J. Kay, S. Y. T. van de Meerakker, E. A. Wade, K. E. Strecker, and D. W. Chandler, *J. Phys. Chem. A* **113**, 14800 (2009).

[16] O. Tkáč, A. K. Saha, J. Onvlee, C.-H. Yang, G. Sarma, C. K. Bishwakarma, S. Y. T. van de Meerakker, A. van der Avoird, D. H. Parker, and A. J. Orr-Ewing, *Phys. Chem.Chem. Phys.* **16**, 477 (2014).

[17] O. Tkáč, A. K. Saha, J. Loreau, D. H. Parker, A. van der Avoird, and A. J. Orr-Ewing, *J.Phys. Chem. A 10.1021/jp5115042* (2015).

[18] O. Tkáč, A. K. Sage , S. J. Greaves, A. J. Orr-Ewing, P. J. Dagdigian, Q. Ma, and M. H. Alexander, *Chem. Sci.* **4**, 4199 (2013).

[19] O. Tkáč, Q. Ma, C.A. Rusher, S.J. Greaves, A.J. Orr-Ewing, and P.J. Dagdigian, *J. Chem. Phys.* **140**, 204318 (2014).

[20] O. Tkáč, Q. Ma, M. Stei, A. J. Orr-Ewing, and P. J. Dagdigian, *J. Chem. Phys.* **142**, 014306 (2015).

[21] O. Tkáč, A. J. Orr-Ewing, P. J. Dagdigian, M. H. Alexander, J. Onvlee, and A. van der Avoird, *J. Chem. Phys.* **140**, 134308 (2014).

[22] E. Habart, M. Walmsley, L. Verstraete, S. Cazaux, R. Maiolino, P. Cox, F. Boulanger, and G. P. Des Forets, *Space Sci. Rev.* **119**, 71 (2005).

[23] S. Maret, A. Faure, E. Scifoni, and L. Wiesenfeld, *Mon. Not. R. Astron. Soc.* **399**, 425 (2009).

[24] K. B. Gubbels, S. Y. T. van de Meerakker, G. C. Groenenboom, G. Meijer, and A. van der Avoird, *J. Chem. Phys.* **136**, 074301 (2012).

[25] A. von Zastrow, J. Onvlee, S. N. Vogels, G. C. Groenenboom, A. van der Avoird, and S. Y. T. van de Meerakker, *Nature Chem.* **6**, 216 (2014).

[26] S. N. Vogels, J. Onvlee, A. von Zastrow, G. C. Groenenboom, A. van der Avoird, and S. Y. T. van de Meerakker, *Phys Rev Lett* **113**, 263202 (2014).

[27] A. T. J. B. Eppink and D. H. Parker, *Rev. Sci. Instrum.* **68**, 3477 (1997).

[28] B. Yan, P. F. H. Claus, B. G. M. van Oorschot, L. Gerritsen, A. T. J. B. Eppink, S. Y. T. van de Meerakker, and D. H. Parker, *Rev. Sci. Instrumen.* **84**, 023102 (2013).

[29] C. H. Yang, G. Sarma, D. H. Parker, J. J. ter Meulen, and L. Wiesenfeld, *J. Chem. Phys.* **134**, 204308 (2011).

[30] C. J. Eyles, D. Phil. Thesis, University of Oxford, 2010.

[31] HIBRIDON is a package of programs for the time-independent quantum treatment of inelastic collisions and photodissociation written by M. H. Alexander, D. E. Manolopoulos, H.-J. Werner, B. Follmeg, P. J. Dagdigian, and others. More information and/or a copy of the code can be obtained from the website http://www2.chem.umd.edu/groups/alexander/hibridon.

[32] C. Rist, M. H. Alexander, and P. Valiron, *J. Chem. Phys.* **98**, 4662 (1993).

[33] L. Wiesenfeld, E. Scifoni, A. Faure, and E. Roueff, *Mon. Not. R. Astron. Soc.* **413**, 509 (2011).

[34] J. Loreau, J. Lievin, Y. Scribano, and A. van der Avoird, *J. Chem. Phys.* **141**, 224303 (2014).

[35] T. R. Phillips, S. Maluendes, A. D. McLean, and S. Green, *J. Chem. Phys.* **101**, 5824 (1994).

[36] A. Offer and D. R. Flower, *J. Phys. B* **22**, L439 (1989).

[37] K. Schreel and J J. ter Meulen, *J. Chem. Phys.* **105**, 4522 (1996).

[38] A. Faure, N. Crimier, C. Ceccarelli, P. Valiron, L. Wiesenfeld, and M. L. Dubernet, *Astron. Atrophys.* **472**, 1029 (2007).

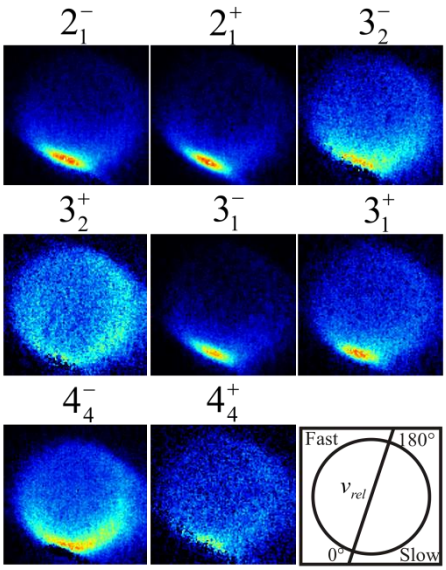

FIG. 1. Experimental velocity map images for the crossed molecular beam scattering of ND_3 with n-H_2 at a collision energy of 580 ± 50 cm^{-1}. The ND_3 was state-selected by a hexapole filter to be almost exclusively in the $j_k^{\pm} = 1_1^-$ state prior to collision and images are shown for eight different final $j'^{\pm}_{k'}$ levels, as indicated by the labels. The orientation of the relative velocity vector v_{rel} is indicated in one panel.

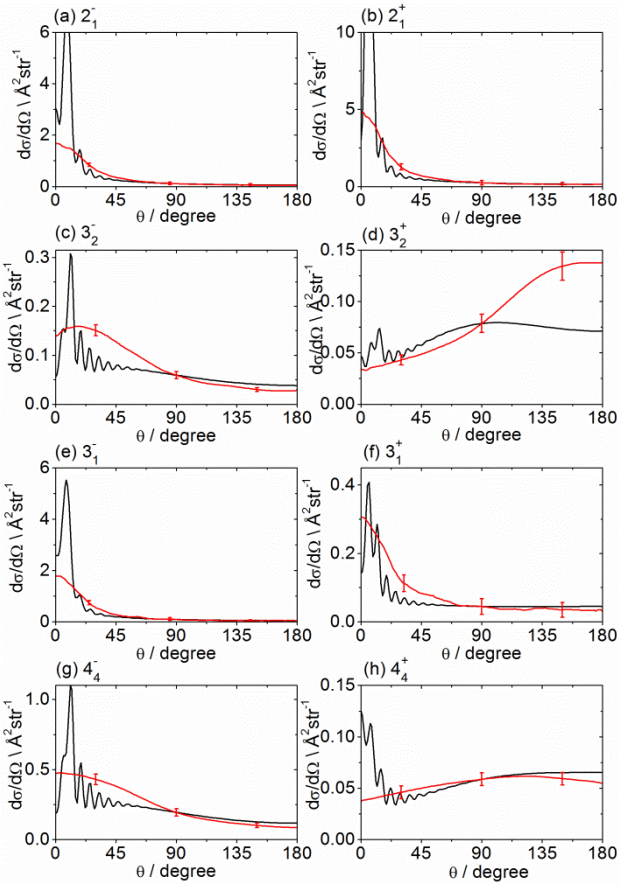

FIG. 2. Experimental (red) and theoretical (black) DCSs for inelastic scattering of ND_3 $j_k^{\pm} = 1_1^-$ with H_2 into various $j'^{\pm}_{k'}$ final levels indicated by the labels. Experimental DCSs were derived from the raw images in Fig. 1 following density-to-flux transformation. The collision energy was 580 ± 50 cm^{-1}.

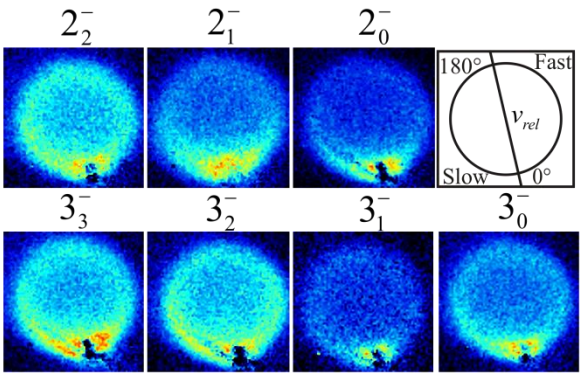

FIG. 3. Experimental velocity map images for the crossed molecular beam scattering of ND_3 with n-H_2. The ND_3 initial state is averaged over + and − symmetry components and rotational levels in accordance with a temperature of ~4 K. The collision energy was 585 ± 50 cm^{-1}.

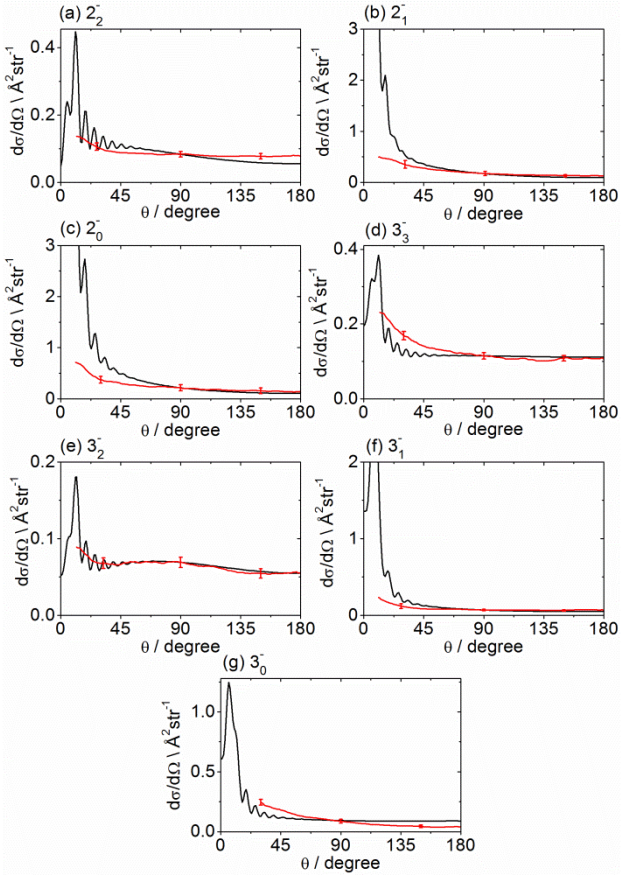

FIG. 4. Experimental (red) and theoretical (black) DCSs for inelastic scattering of ND_3 with H_2 into various final j'_k, levels with − symmetry. The hexapole state selection process was not used for this experiment. Experimental DCSs were derived from the raw images in Fig. 3 following density-to-flux transformation. The collision energy was 585 ± 50 cm^{-1}.

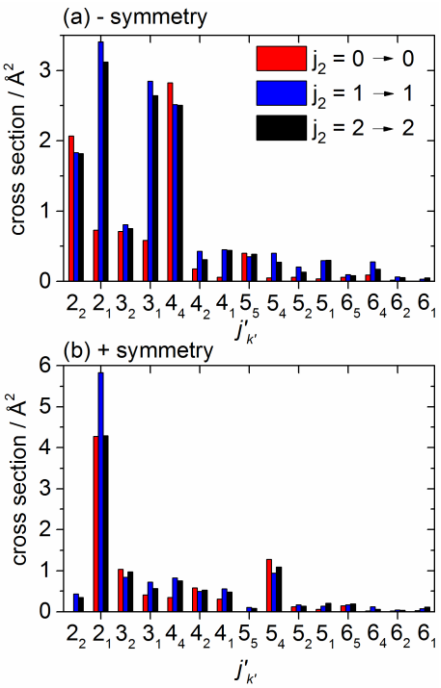

FIG. 5. Calculated integral cross sections for rotationally inelastic scattering of ND_3 out of the 1_1^- level into various final levels with (a) – inversion symmetry and (b) + inversion symmetry for collisions with H_2 in j_2= 0, 1 and 2 rotational levels. The ICSs are plotted for collisions that conserve j_2. The collision energy was 580 cm^{-1}.

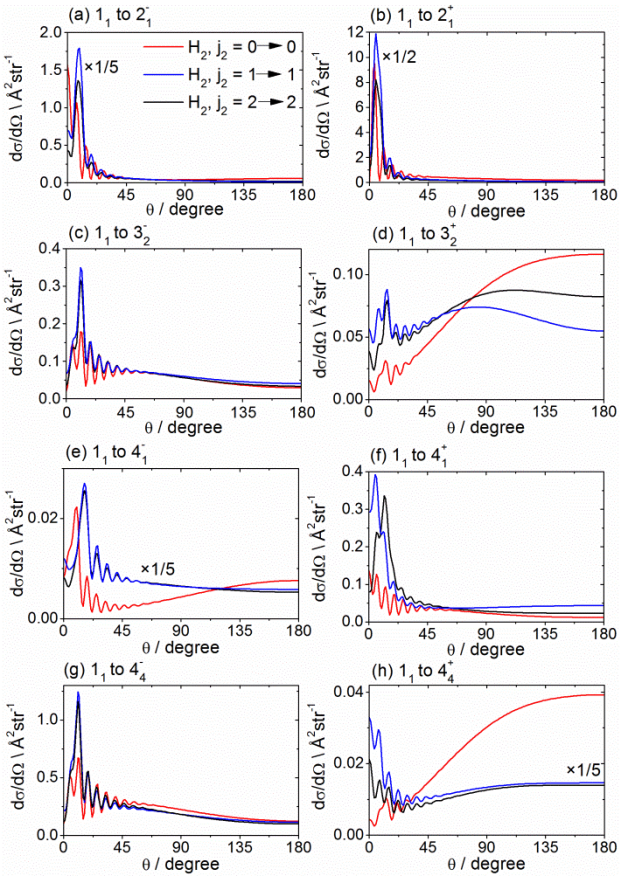

FIG. 6. Computed state-to-state DCSs for inelastic scattering of ND_3 from the 1_1^- rotational level into selected final $j'^{\pm}_{k'}$ levels. The collision partner was H_2 and the collision energy was 580 cm^{-1}. The individual curves are ND_3–H_2 DCSs for which the initial rotational level j_2 of the H_2 collider was 0, 1 and 2, and remained the same after the collision. In some panels, the $j_2 = 1 \rightarrow 1$ and $j_2 = 2 \rightarrow 2$ DCSs have been multiplied by the angle-independent scaling factor indicated on the plot.

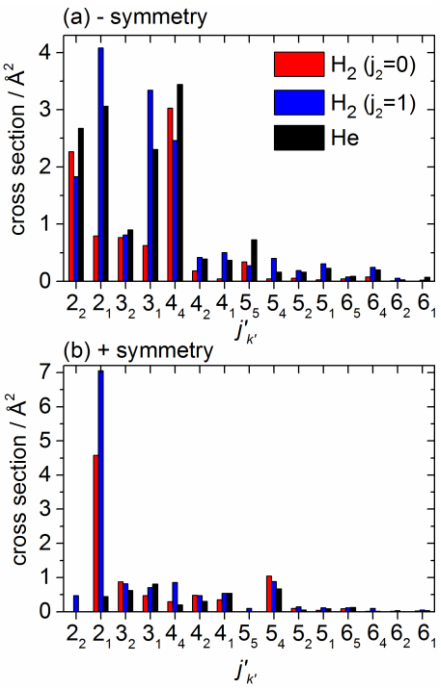

FIG. 7. Comparison of calculated integral cross sections for rotationally inelastic scattering of ND_3 out of the 1_1^- level into various final levels with (a) – inversion symmetry and (b) + inversion symmetry for collisions with H_2 in j_2= 0 and 1 rotational levels and with He. The collision energy used for all calculations was 430 cm^{-1}.

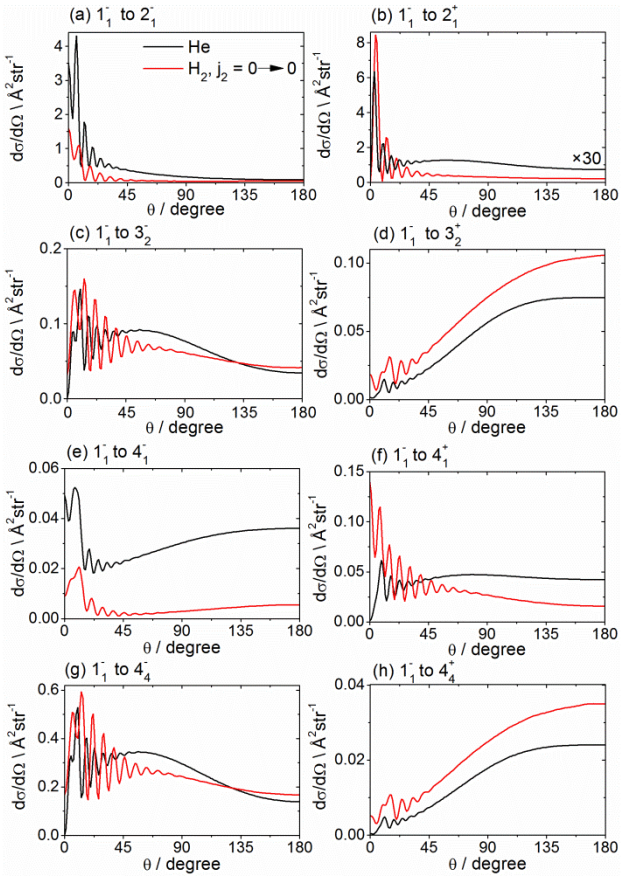

FIG. 8. Comparison of calculated differential cross sections for rotationally inelastic scattering of ND_3 out of the 1_1^- level into various final levels with (a) – inversion symmetry and (b) + inversion symmetry for collisions with H_2 in the j_2= 0 rotational level (red) and He (black). The collision energy for all calculations shown was 430 cm^{-1}.